PAPER

Check for updates

Cite this: *Nanoscale*, 2024, **16**, 2012

Formation and properties of spindle-shaped aragonite mesocrystals from Mg-bearing solutions†

Zsombor Molnár, [iD] *[a,b] Péter Pekker,[a] Aleksander Rečnik[c] and Mihály Pósfai [iD] [a,b]

The formation of aragonite under ambient conditions is typically linked to Mg-rich aqueous environments. The grains that form in such environments show peculiar properties such as aggregate-like appearance and mesocrystalline character. We tested the effect of dissolved Mg^{2+} ions on the formation of aragonite mesocrystals by synthesizing aragonite with an automatic titrator at constant pH and at different dissolved Mg : Ca ratios, and by studying the properties of the precipitated material with various scanning transmission electron microscopy (STEM) techniques. At all studied Mg : Ca ratios the firstly condensed carbonate phase was Mg-bearing amorphous calcium carbonate (Mg-ACC) that transformed into aragonite during the synthesis experiments. The aragonite grains had typically aggregate-like appearance and spindle shapes, with the external morphologies of the spindles unaffected by variation in solution chemistry. The alignment of the nanocrystals within the aggregates was crystallographically highly coherent, the [001] directions of nanocrystals showing only a small misorientation with respect to one another; however, both parallel and twin assembly of neighbouring crystals occurred. An increase in the dissolved Mg concentration decreased the crystallographic coherence between the aragonite nanocrystals, suggesting an important role of Mg^{2+} ions in the assembly of aragonite spindles. Whereas the mesoscale-ordered arrangement of nanocrystals implies a particle-mediated assembly, the observed differences in particle size and composition between the amorphous precursor and the crystalline end-product suggest that the crystallization includes at least partial dissolution and re-precipitation. These findings provide insight into the formation of aragonite and could contribute to the understanding of important aspects of the formation of mesocrystals and hierarchically structured biogenic minerals.

Introduction

Among the three anhydrous $CaCO_3$ polymorphs, orthorhombic aragonite is typically described as the most stable phase at high pressure.[1] Nevertheless, it forms abundantly under surface conditions, typically in aqueous environments characterized by either high dissolved Mg^{2+} concentrations or elevated temperatures.[2–5] Despite its abundance and geochemical importance,[6,7] the abiotic formation of aragonite is less studied than that of calcite.[8]

[a]University of Pannonia, Research Institute of Biomolecular and Chemical Engineering, Nanolab, Egyetem st. 10, 8200 Veszprém, Hungary. E-mail: molnar.zsombor@mk.uni-pannon.hu
[b]HUN-REN-PE Environmental Mineralogy Research Group, Egyetem st. 10, 8200 Veszprém, Hungary
[c]Jožef Stefan Institute, Department of Nanostructured Materials, Jamova cesta 39, 1000 Ljubljana, Slovenia
†Electronic supplementary information (ESI) available: Uploaded document and movies. See DOI: https://doi.org/10.1039/d3nr04672a

Aragonite particles that form in Mg-rich aqueous media have a peculiar spindle-like appearance. They are composed of a large number of nanosized crystals that collectively produce single-crystalline electron diffraction patterns, implying a mesocrystalline character.[9–12] These properties have been observed in both natural[13] and synthetic samples, the latter including both abiotically[6,9,11,14–23] and biomimetically synthesized aragonite.[12,24–27] Whether they formed homogeneously[10] or in the presence of additives (such as polyaspartic and amino acids,[28] solely amino acids,[26] polyamides,[12] or swelling clay minerals[11]), the mesocrystalline characters of aragonite aggregates were similar. Despite their widespread occurrence, the formation mechanism of aragonite spindles is not clearly understood, even though such an understanding could shed light on important aspects of the formation of mesocrystals.

The formation of mesoscopically structured crystals (mesocrystals), especially the cohesion between their fundamental units is a widely studied yet puzzling phenomenon.[29] According to the original definition,[30] mesocrystals form by

the attachment of nanocrystals, a process regulated by the interactions of their different facets, and potentially mediated by organic polymers or gels.[31–33] However, Zhu *et al.*[34] suggested that mesocrystals could alternatively be produced *via* conversion of amorphous nanoparticles into nanocrystals near mineral surfaces, in a process that involves both dissolution–re-precipitation and oriented attachment. Regardless of their assumed formation mechanism, the properties of mesocrystals differ from those of bulk single crystals,[35] *e.g.*, have larger surface area and porosity, making them effective substrates for adsorption.[36]

With respect to the possible role of an amorphous precursor in the formation of aragonite mesocrystals, Walker *et al.*[10] performed cryo-TEM analysis on freshly precipitated aragonite, synthesized in ethanol-rich aqueous media. They showed the formation of spindle-shaped aragonite mesocrystals in co-occurrence with ACC. The authors suggested that the formation of the spindles was initiated by the aggregation of ACC nanoparticles, and the crystallization of aragonite started within the amorphous aggregate from independent centres, with the amorphous to crystalline transformation taking place in solid state. Huang *et al.*[26] and Nahi *et al.*[12] studied the effect of amino acids and the combined effects of polyamines and dissolved Mg^{2+} ions on the formation of aragonite. Both studies reported similar aggregates of aragonite nanocrystals with a typical spindle-shaped external morphology, and observed the presence of small ACC globules on the surfaces or even within the cavities of aragonite aggregates. Based on the crystallographically highly oriented assembly of aragonite nanocrystals, the authors of both studies concluded that the spindle-shaped aragonite aggregates formed *via* the oriented attachment of nanocrystals. Nevertheless, they assumed that ACC was a precursor of aragonite.

While there are several reports in the literature on the formation of spindle-shaped aragonite aggregates, only a few studies addressed the specific role of Mg^{2+} ions.[6] Since Mg^{2+} is present (in highly variable concentrations) in almost all types of natural waters, it probably affects contemporary aragonite formation in various environments. In addition, the variation of Mg : Ca ratio over the history of Earth in both marine[37] and freshwater systems[38] serves as a proxy for environmental changes; thus, knowing the roles of Mg in aragonite formation has importance for paleoenvironmental reconstructions as well.

In this work, laboratory studies were conducted under environmentally relevant conditions to examine the mechanism of aragonite formation in alkaline (pH 9.00), low-ionic-strength (0.02–0.08 M), Mg-rich aqueous media at ambient temperature (20 °C), with a focus on the transition of amorphous precursors into crystalline phases and the roles of dissolved Mg^{2+} ions. The experiments were conducted with various dissolved Mg : Ca ratios and the products were studied using transmission electron microscopy (TEM) techniques. We demonstrate that the firstly precipitated Mg-bearing ACC precursor transforms rapidly into aragonite, and aragonite mesocrystals form by attachment and subsequent crystallization of

amorphous particles on the surfaces of crystalline nuclei. Further, we show that an increase of the Mg : Ca ratio slows the formation of aragonite and affects the size and orientation of the nanocrystalline building blocks within mesocrystals.

Materials and methods

Synthesis of aragonite

Aragonite mesocrystals were synthesized from aqueous solutions by titrating a carbonate buffer solution with mixtures of Mg and Ca chloride solutions under ambient conditions and constant pH. Firstly, 20 mL, 0.01 M Na_2CO_3 buffer solution was prepared, and the pH set to 9.00 by adding a sufficient amount of 1 M HCl. In order to study the effect of Mg^{2+} ions, we prepared the Mg-rich titrant solutions as mixtures of aqueous $MgCl_2$ and $CaCl_2$ solutions with 0.01 : 0.01, 0.04 : 0.01, 0.06 : 0.01 and 0.08 M : 0.01 M dissolved Mg : Ca ratios, respectively. For the preparation of the solutions, we used analytical graded reagents and double distilled ultra-pure water with 18.2 MΩ resistivity as a solvent.

The titrants were dosed into the buffer solutions by a Metrohm 805 Dosimat automatic titrator. The dosing unit was 5 μL and the dosing speed 0.05 mL min^{-1}. The pH of the solution was kept constant at 9.00 (±0.02) by the dynamic titration of 0.1 M NaOH with a Metrohm 888 Titrando instrument, and measured using a combined, glass pH electrode, with a measuring interval of 2 s. The reactions were monitored by the amount of the dosed NaOH solution. The point of nucleation of solid phases was defined by the concentration where the shape of the titrant curve of the NaOH solution changed from linear to exponential. Each experiment was repeated five times, and the results we present are the mean values for each dissolved Mg : Ca ratio.

The saturation indices (SI) of calcite, aragonite, ordered dolomite and Mg-bearing ACC (Mg-ACC) phases were calculated using the PHREEQC software.[39] The known ionic compositions of the solutions at the point of nucleation, and the previously reported $\log(K_{sp})$ values of calcite, aragonite, dolomite, pure-ACC and Mg-ACC were used for the calculations. References for the applied $\log(K_{sp})$ values are included in Fig. S1.†

In parallel experiments, we sampled the precipitated materials first at the point of nucleation, then at the point where the volume ratio of the titrant and buffer solutions reached 1, and finally after aging for 2 months. Sampling was done by filtering the whole solution through a 0.45 μm MCE polymer membrane filter with a vacuum pump, then washing the filtered solid materials with 20 mL isopropanol in order to avoid their crystallization upon drying. Four specimens were prepared and analysed for each used Mg : Ca ratio, in order to make sure that incidental drying artefacts (such as individual NaCl or $MgCl_2$ crystals) are recognized. We did not observe the occurrence of such salt phases on the surfaces or in the pores of aragonite crystals.

Material characterization

Samples for transmission electron microscopy (TEM) analyses were prepared by gently touching the surface of the wet filter paper with a carbon-coated lacey Cu grid immediately after the filtering procedure, and drying the grid at room temperature. For TEM analysis we used a Thermo Fisher Talos F200X G2 scanning transmission electron microscope (STEM) that could be operated in both conventional and scanning TEM mode, at 200 kV accelerating voltage. We studied the morphologies of solid particles in bright-field (BF) images, selected-area electron diffraction (SAED) patterns and high-resolution TEM (HRTEM) images for structural characterization of the grains. The beam current was around 80 pA in TEM mode. Elemental maps were obtained in STEM spectrum imaging mode by collecting energy-dispersive X-ray (EDX) spectra in each pixel of the image, using a four-detector SuperX Si drift detector system. In STEM mode the beam current was around 200 pA. The obtained data were processed and evaluated using Velox 2.14 software.

Electron tomography measurements were carried out in STEM mode using the high-angle annular dark-field (HAADF) detector for imaging. The chosen grain was tilted in 1° steps in a tilt series between −62° to 60°. We used Inspect3D software for 3D reconstruction and the Avizo software for the visualization of particle morphologies.

Results

In our experiments designed to precipitate aragonite a carbonate buffer was titrated with mixtures of Mg and Ca chloride solutions, while the pH was kept constant by the dosing of NaOH. The measured curves of the dosed amount of NaOH solution showed a typical sigmoidal shape in each experiment, indicating a pH change within the solution that was balanced by the addition of the NaOH titrant (Fig. 1A). The general equation of solid $CaCO_3$ formation is expressed by eqn (1).

$$Ca^{2+} + HCO_3^- \rightleftarrows Ca^{2+} + CO_3^{2-} + H^+ \rightarrow CaCO_3 + H^+ \quad (1)$$
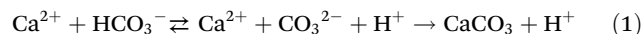
According to the law of mass action and the principle of mass preservation, HCO_3^- is the dominant form of carbonate at pH 9.00 (92 mol%), and CO_3^{2-} occurs as a minor species (5 mol%). When HCO_3^- dissociates into CO_3^{2-} and solid $CaCO_3$ forms, H^+ ions are liberated that decrease the pH of the solution. Adding NaOH maintained the initial pH 9.00, and the amount of added NaOH solution provided a proxy for identifying the nucleation of $CaCO_3$. We refer to the point where the increment of the dosed NaOH solution started to increase as the point of nucleation.

Increasing the dissolved Mg : Ca ratio shifted the point of nucleation slightly, lengthening the pre-nucleation limb of the titration curves (Fig. 1A); thus, the solid phases formed at larger ionic strength (at 0.024, 0.031, 0.037 and 0.071 M for the 1 : 1, 4 : 1, 6 : 1 and 8 : 1 dissolved Mg : Ca ratios, respectively; see Fig. S1†). We used the ionic compositions of the solutions at the point of nucleation for calculating the saturation indices (SI) of possible solid phases (Fig. 1B). The SIs suggested that the solutions were supersaturated with respect to calcite, aragonite and dolomite, slightly supersaturated or undersaturated with respect to pure ACC, depending on the used $\log(K_{sp})$ value (not shown in Fig. 1B), but undersaturated with respect
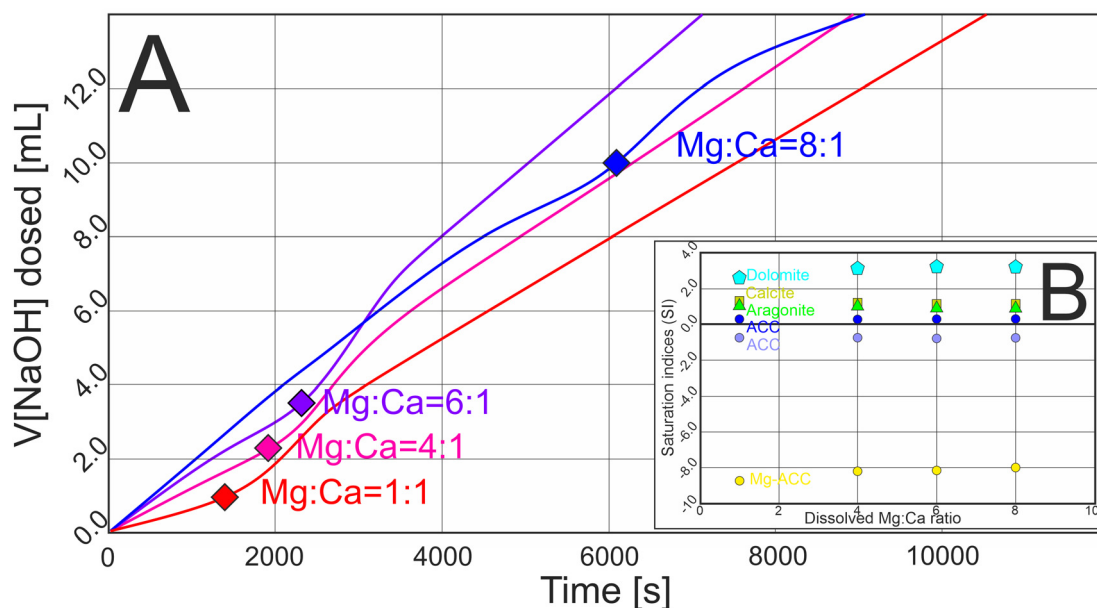
Fig. 1 (A) Measured curves of the amount of dosed NaOH solution for four carbonate precipitation experiments with different dissolved Mg : Ca ratios. On each curve a rectangle marks the point where the increment of the dosed solution started to increase, indicating the starting point of the nucleation of carbonate solids (for details see Fig. S1†). (B) Calculated saturation indices (SI) of calcite, aragonite, dolomite, ACC (using two different K_{sp} values) and Mg-ACC (50 mol% Mg content) at the point of nucleation. The SIs indicate that the solution was undersaturated with respect to Mg-ACC and around the saturation state with respect to ACC.

to Mg-bearing ACC in every case (assuming 50 mol% Mg content in the amorphous phase and using the K_{sp} value of Purgstaller *et al.*[40]). The calculated SIs for calcite and aragonite were essentially unaffected by the Mg : Ca ratio (1.2 and 1.1, respectively) (Fig. 1B and S1†).

TEM study of the samples that were taken from the solutions immediately after the point of nucleation revealed coexisting Mg-ACC and aragonite particles. Mg-ACC particles were a few tens of nm large, their shapes spherical or elongated-globular; some individual globules also occurred, but they typically formed small groups in intimate association with aggregates of aragonite nanocrystals at every used Mg : Ca ratio (Fig. 2A). As expected, the groups of Mg-ACC showed amorphous character in both SAED patterns and fast Fourier transforms (FFTs) obtained from HRTEM images, producing diffuse intensity maxima (see the FFT of area 1 in Fig. 2A; Fig. S2 and S3†) with *d*-values corresponding to those reported by Molnár *et al.*[41] Mg-ACC particles contained a significant amount of Mg (Fig. 2B–C and Fig. S3†) but their Mg : Ca ratio was lower than that of the solution (*i.e.*, 0.45–0.55 *vs.* 4, respectively). On the other hand, no Mg could be detected in the aragonite aggregates, suggesting that Mg is not incorporated into aragonite even at an initial stage of formation (Fig. 2C). The smallest, presumably incipient aragonite particles were already aggregates that consisted of <10 nm nanocrystals; the entire aggregate produced SAED and FFT patterns

reminiscent of single-crystal diffraction (see FFT of area 2 in Fig. 2A). Images such as in Fig. 2A and 3 suggested that aragonite aggregates grew by the attachment of Mg-ACC. Even though we sampled the solution at the point of nucleation, irregular-shaped aggregates (as in Fig. 2A) were rare (we observed about ten particles); instead, the typical aragonite aggregates resembled spindles (Fig. 3A, B and 4A), with specific morphologies and structures.

Aragonite spindles had uniform aspect ratios (length to width, l/w = 3.6), independent of the Mg : Ca ratio of the solution (Fig. 4A and B; 15 particles were measured for each dissolved Mg : Ca ratio). The combination of granular texture and single-crystal-like diffraction displayed by the spindles implied a mesocrystalline character. High-resolution study of spindle nanotexture showed that the spindles were composed of few tens-of-nm-large nanocrystals that maintained their mutual orientation relationship with respect to one another, with their *c*-axis approximately aligned in the direction of the long axis of the spindle (Fig. 4A and 5A–B). The interfaces between the individual nanocrystals were indistinct, with either amorphous material or pores separating the crystalline units, as is characteristic for mesocrystal assemblies.

As is also typical for mesocrystals, the alignment of the constituting nanocrystals is imperfect. Typical SAED patterns suggest angular dispersions of nanocrystals, manifested in the intensity maxima appearing as short arcs (Fig. 5A and B). The
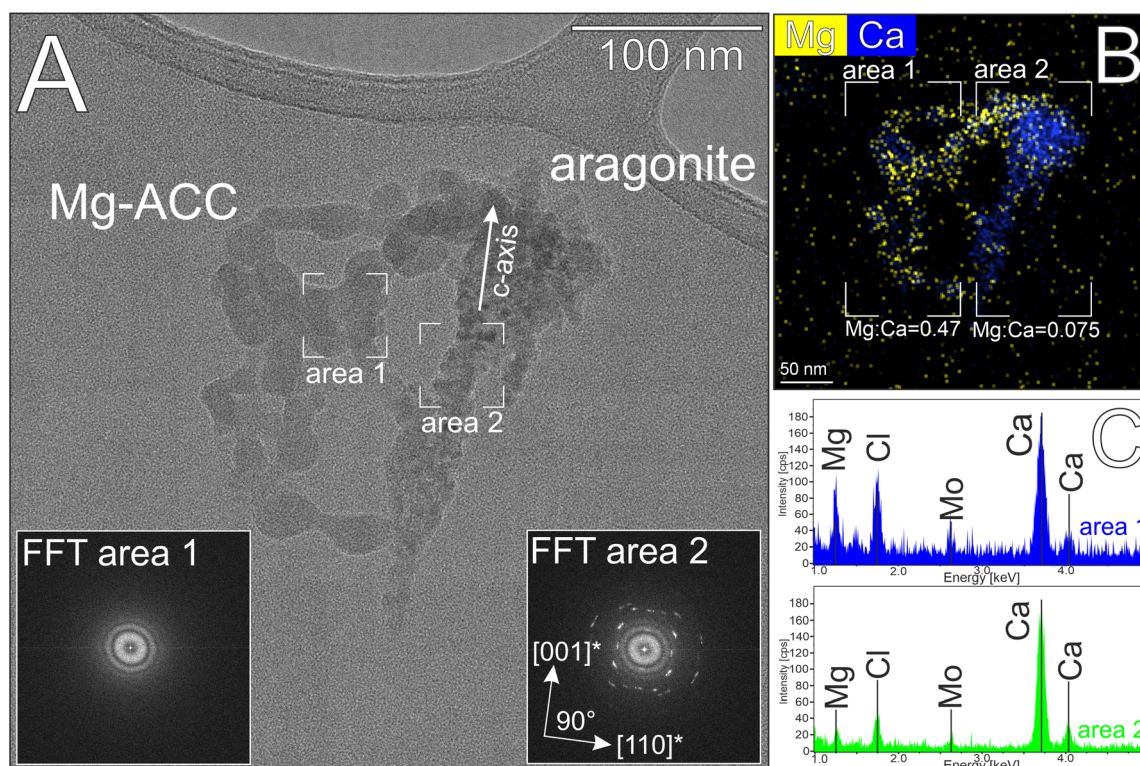
Fig. 2 Globular Mg-ACC particles with aragonite crystals. (A) HRTEM image with the corresponding FFTs of Mg-ACC and aragonite particles in the inserts, from the areas marked in the main panel. (B) STEM EDX elemental map and (C) corresponding EDX spectra extracted from the marked areas, showing significant Mg in Mg-ACC and almost none in aragonite. The small Mo K_α peak arises from stray radiation from the sample holder.
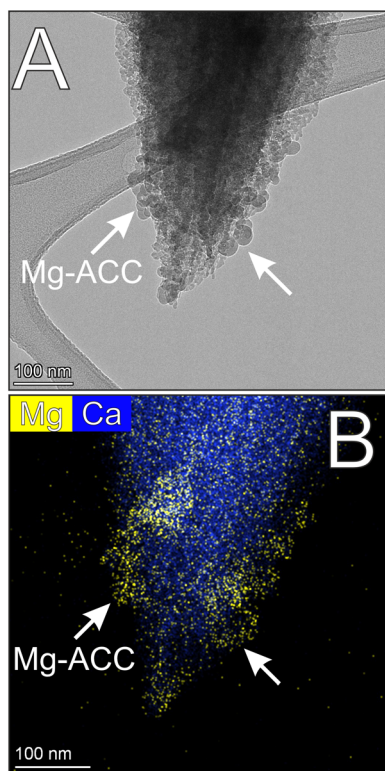
Fig. 3 Globular Mg-ACC particles on spindle-shaped aragonite aggregates. (A) BF image and (B) STEM EDX elemental map from the same area of the same particle, suggesting that Mg-ACC globules (marked by white arrows) appear only on the surface of the aragonite spindle.

lengths of the arcs belonging to particular intensity maxima, *e.g.*, to the 002 reflection, increase with the Mg : Ca ratio of the solution (with the arc angle changing from 5 ± 0.5° to 8 ± 0.3° as the Mg : Ca ratio increases from 1 : 1 to 8 : 1) (Fig. 5C; 10 particles were measured for each dissolved Mg : Ca ratio). The trend of increasing misalignment of nanocrystals is probably related to the decrease of particle size with increasing Mg : Ca ratio (Fig. 4C). We measured the perimeters of the nanocrystals in random positions within the aggregates. The average perimeters of the nanocrystals were 122, 84 and 44 nm in the spindles precipitated from solutions with 1 : 1; 4 : 1 and 8 : 1 dissolved Mg : Ca ratios, respectively (Fig. 4C; 80 particles were measured for each dissolved Mg : Ca ratio).

SAED patterns and FFTs of HRTEM images obtained from aragonite spindles often show double periodicity along the [110]* directions (Fig. 5D–F; Fig. S4†). Reflections appear that are incompatible with the conventional *Pmcn* space group of aragonite, since they would have to be assigned non-integer indices (*e.g.*, $\frac{1}{2},\frac{1}{2},0$). Similar reflections have been observed in synthetic aragonite, and interpreted as superstructure reflections.[42] In places HRTEM images show neighbouring nanocrystals in [100] and [1$\bar{1}$0] orientations (Fig. 6), with their [001] directions almost parallel, suggesting a twin relationship between the two crystals. Based on our observations, two self-assembly modes, (i) lateral (110)[001]‖(110)[001] and (ii) twin
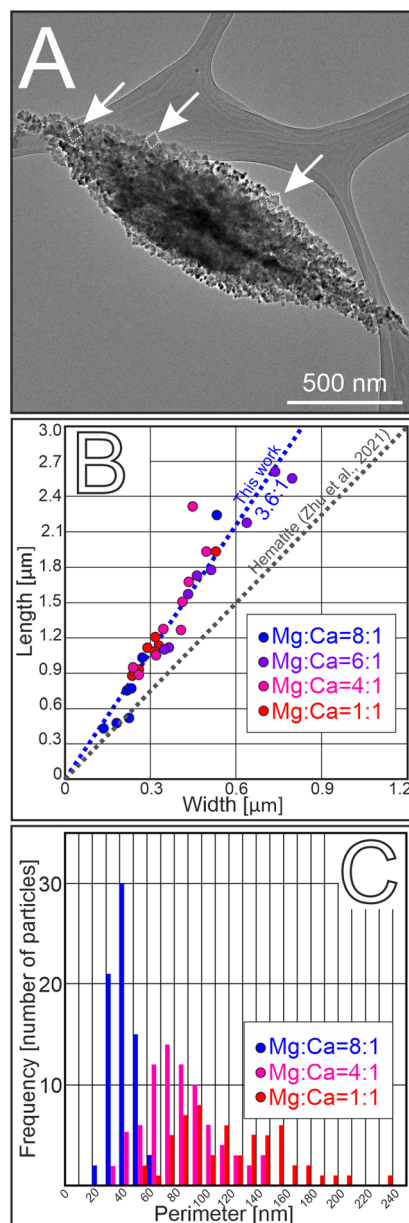

Fig. 4 Morphology of spindle-shaped aragonite. (A) BF TEM image showing that the particles have aggregate-like appearance, consist of a large number of nanocrystals and have typical spindle-like morphology. Individual aragonite nanocrystals are framed by white dashed lines and marked by white arrows. (B) The external morphology of the spindle-like aggregates was uniform at every used dissolved Mg : Ca ratio, with the aspect ratio (length-to-width) of the aggregates around 3.6 : 1 (15 particles were measured for each dissolved Mg : Ca ratio). (C) The sizes of the individual nanocrystals (characterized by their perimeter) that build up the aggregates decreased with increasing dissolved Mg : Ca ratio (80 particles were measured for each dissolved Mg : Ca ratio).

(110)[001]‖(110)[00$\bar{1}$] are identified. Similar observations were reported for other minerals, such as magnetite[43] and rutile.[32] We suspect that the above two structural features, *i.e.*, the appearance of half-integer reflections and the presence of twinning, might be related; however, conclusive evidence for this is still lacking.
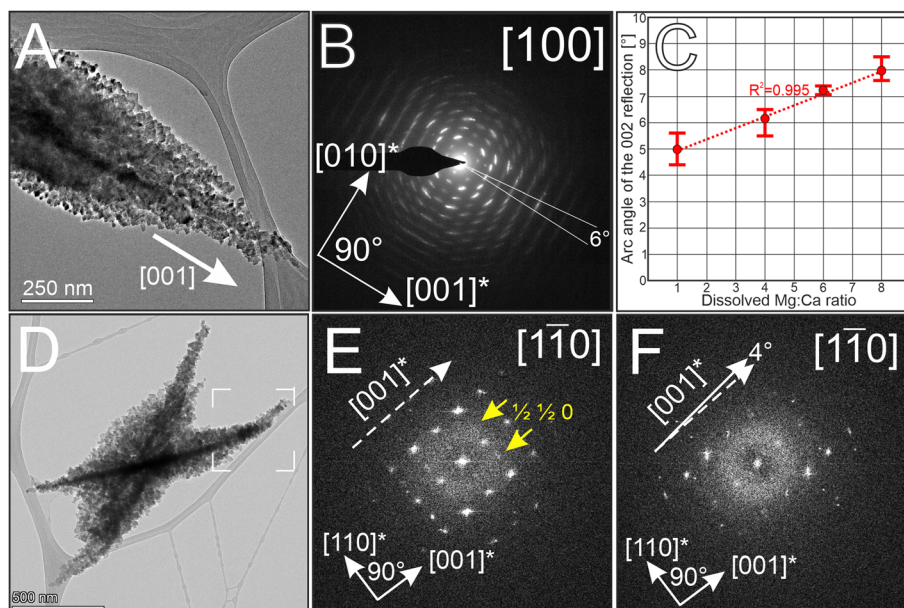
Fig. 5 Structure analysis of spindle-shaped aragonite aggregates. (A) BF image of a spindle with (B) corresponding SAED pattern that shows elongated, arc-shaped intensity maxima. (C) The arc length of the 002 refection increased with increasing dissolved Mg : Ca ratio (10 particles were measured for each dissolved Mg : Ca ratio). (D) BF image of a spindle with (E) and (F) corresponding FFTs (the marked area shows the places of the two HRTEM images from where the FFTs were calculated, for the original HRTEM images see Fig. S3†), displaying small misorientations between the constituent nanocrystals and the appearance of extra periodicity (marked by yellow arrows) that is inconsistent with the structure of aragonite.
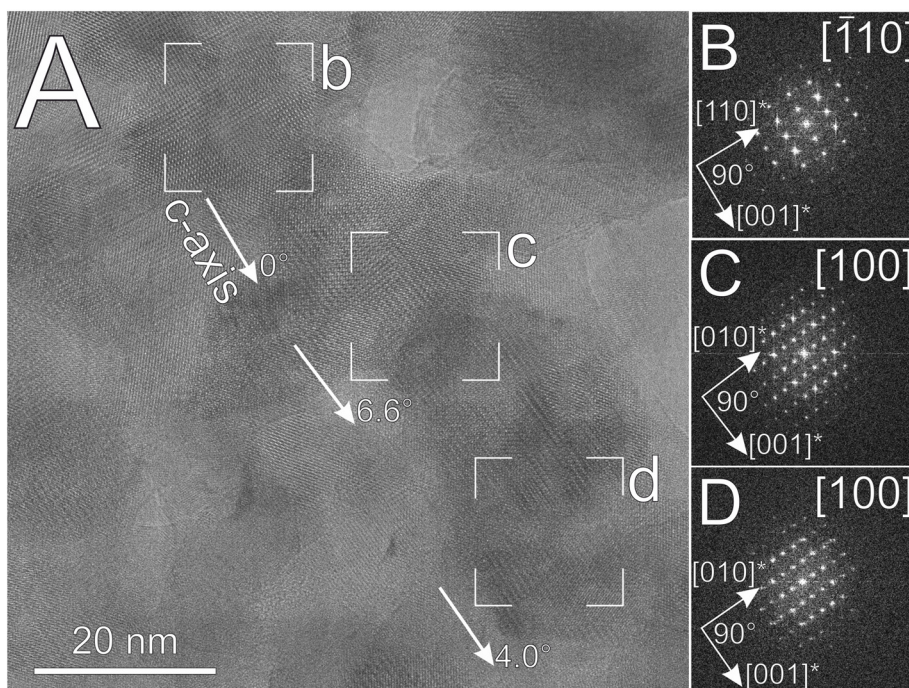

Fig. 6 (A) HRTEM image with (B), (C) and (D) corresponding FFTs, obtained from the external part of an aragonite spindle. Two main projections, [$\bar{1}$10] and [100] were observable for the nanocrystals but their [001]* directions were almost perfectly aligned.

The typical spindle-like morphology of the aragonite aggregates is preserved up to an equal titrant to buffer volume ratio (approximately 3 hours after the nucleation). However, intergrown spindles and more complex, star-like aggregates become more abundant with processing time (Fig. 7A). STEM tomography shows a lamellar morphology of the intergrown spindles (Fig. 7B and Fig. S5 and S6 movies 1–2†). The angles between the long axes of intergrown spindles seem to be
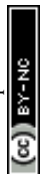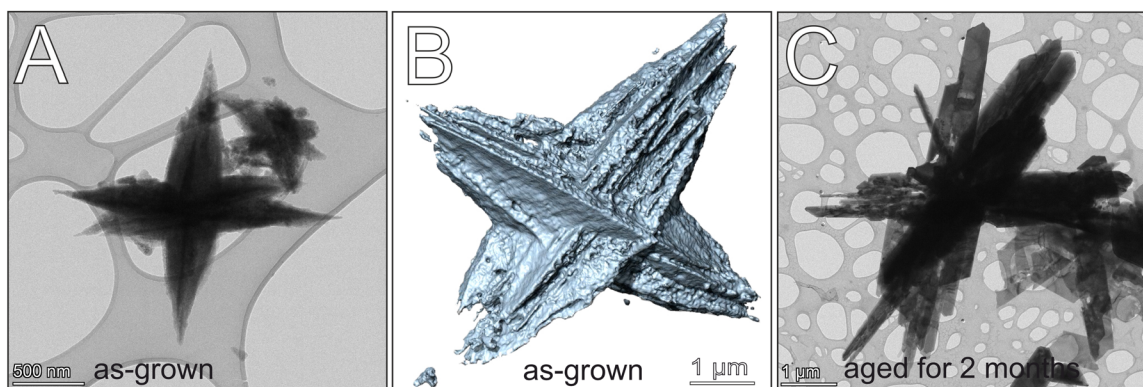
Fig. 7 Size and morphology changes during the aging of spindle-shaped aragonite aggregates. (A) TEM BF image and (B) tomographic reconstruction of freshly precipitated aragonite particles consisting of two or more intergrown spindles. (C) TEM BF image of aragonite crystals aged for two months; the mesocrystal-like appearance of the firstly formed aragonite particles vanished and perfect single crystals appeared.

specific at first glance, potentially suggesting a twin relationship; however, when measured from the STEM tomographic reconstruction the angles appear to be incidental (Fig. S5†). The tomographic measurements also confirm the presence of holes of various sizes (up to tens of nm) within the aragonite aggregates, located at random positions (Fig. 7B and S6 movie 3†).

After two months aging, the spindles transformed into assemblies of several-μm-long, well-facetted, lath-shaped aragonite crystals (Fig. 7C) that typically showed the half-integer reflections when viewed along [1$\bar{1}$0] projection (Fig. S7†). These aggregates were loosely bound, and after 120 s ultrasonication disaggregated into individual aragonite crystals.

Discussion

Our study confirmed the results of earlier research regarding two important aspects of aragonite formation, namely that (i) increasing the Mg : Ca ratio of the solution delays the formation of the first solid, and (ii) Mg-ACC is a precursor of aragonite. In our experiments nucleation started at increasing ionic strength as the dissolved Mg : Ca ratio increased (Fig. 1A and S1†), as was also observed earlier,[23,44] and the firstly formed phase was Mg-ACC that later transformed into aragonite (Fig. 2). In general, the formation of crystalline $CaCO_3$ is a multistep process involving both liquid and solid precursors. The first solid is typically ACC that transforms into less soluble, crystalline phases via either solid-state transformation or dissolution and re-precipitation processes (DRP), or a combination of both.[45] Both in situ TEM[46] and SAXS/WAXS[45] experiments showed that in the absence of Mg^{2+} ions ACC particles could transform into vaterite and then to calcite, in agreement with the Ostwald-step rule and as the solubility of the given $CaCO_3$ phases would suggest. As discussed above, in our experiments the solid-state transformation of Mg-ACC can be excluded. On the other hand, a scenario involving its dissolution offers an explanation for the polymorph selection.

Once the dissolution of Mg-ACC has started and the dissolved Ca^{2+} concentration reaches supersaturation with respect to both calcite and aragonite, a new $CaCO_3$ phase is formed. However, the dissolved Mg^{2+} ions kinetically hinder or decelerate the formation of Mg-bearing calcite crystals via poisoning the growth of calcite nuclei,[2,47] thereby enhancing the formation of aragonite,[2] the second-least-soluble form of $CaCO_3$.

Morphological features of aragonite spindles (Fig. 4) and the specific crystallographic orientation relationship between their component nanocrystals (Fig. 5 and 6) imply that the spindles formed by particle attachment, i.e., in a non-classical crystallization process, as was also suggested by previous authors.[6,12,15,26,35] The formation of mesocrystals via the attachment of crystalline nanoparticles in a crystallographically co-aligned fashion was widely described, e.g., in titanium oxides,[32,48] iron oxides,[34,49,50] and calcium sulphates.[51,51,52] However, the rapid oriented attachment of aragonite nanocrystals is unlikely after their burst nucleation at room temperature, in a weak electrolyte solution, at slightly alkaline pH; moreover, we never observed individual aragonite nanocrystals in our samples. On the other hand, at the initial stages of spindle formation the presence of Mg-bearing ACC on the surfaces of aragonite spindles appeared to be common (Fig. 2 and 3), whereas this phenomenon was absent with increasing reaction time. These observations indirectly suggest that the aragonite spindles grew by the attachment of Mg-ACC particles.

For the growth of aragonite spindles previous studies proposed three models, all of which assumed a particle-mediated growth processes, with their main differences being whether amorphous or crystalline particles are assembled, and where the amorphous to crystalline transformation happens relative to the growing spindles. Walker et al.[10] suggested that assembly of amorphous particles is followed by their transformation into aragonite in solid state. Others[12,15,26,36] claimed that the growth of the spindles is dominated by the attachment of ACC onto the surfaces of pristine aragonite nanocrystals, with the ACC transforming in solid state and inheriting the structure and orientation of the substrate aragonite nanocrystal. A third

model[16] suggested that crystalline aragonite nanoparticles attached to one another in a crystallographically well-oriented manner; nevertheless, even in this case the ACC was considered a precursor phase. Our observations support the model by Zhu *et al.*[34] concerning the attachment of Mg-ACC to pre-existing aragonite; however, we assume the amorphous to crystalline transition takes places *via* a dissolution–reprecipitation process, as discussed above. While the attachment of Mg-ACC to preformed aragonite aggregates is well documented by our TEM images, much less is known about the nucleation of the first nanocrystals. Images obtained from the smallest, presumably incipient aragonite aggregates (Fig. 2A) suggest that once nanocrystals form, they align along the *c*-axis (Fig. 2) according to an oriented self-assembly mechanism.[32,34,53]

Compared to the oriented attachment of nanocrystals that are homogeneously precipitated from supersaturated solutions,[48,53] the driving forces behind interface-driven nucleation[34] are less understood. According to our observations, Mg-ACC is continuously dissolving, thus losing its initial Mg content. Along with this process, new aragonite nanocrystals form in the vicinity of spindles. It remains to be understood why the nanocrystals form in the vicinity of mineral surfaces (*i.e.*, not in direct contact with them), and why they are assembled into mesocrystals instead of growing into single crystals *via* classical crystal growth.[54] In fact, the observed mechanism is not too different from conventional mesocrystal assembly, where nanocrystals are attracted and aligned *via* van der Waals (vdW) forces, and surface interactions control their oriented attachment.[33] However, in the case of aragonite spindles these vdW forces may be also involved in the oriented near-surface crystallization of the nanoparticles, when the amorphous precursor reaches the immediate vicinity of the mineral surface.[34] At the same time, surface ligands hold the new nanocrystals in a stable separation from the existing crystalline surface, preventing their merging *via* classical pathways.[33] According to the Lifshitz formulation of vdW interactions,[54] orientational dependency originates from the anisotropy of bulk dielectric properties defined by structure-dependent dielectric tensors of interacting materials, which conduct force fields that convey structural information beyond the phase boundary, thus aligning the interacting nanocrystals.[32] Such forces may be responsible for the oriented, near-surface amorphous-to-crystalline transformation, as was also observed for iron oxides.[34] The misalignment of nanocrystals and the mesocrystalline structure (Fig. 5 and 6) of the aragonite spindles support the mechanism of oriented near-surface nucleation.

The highly anisotropic shape of the spindles suggests that the rate of particle attachment is higher along the [001] direction than perpendicular to it. Some authors observed that the amorphous particles prefer a distinct direction with respect to their attachment;[55] indeed, newly formed crystalline particles were shown to preferably attach to the tips of the spindles.[34] This could be explained by the tendency of the material to maintain its equilibrium crystal shape, as has also been observed in other mesocrystals.[56] The measured uniform length-to-width ratio of the spindles (3.6 : 1) suggests that this morphology is typical for the early stages of aragonite formation, and the dissolved Mg content does not affect the external shape of the aggregates (Fig. 4B).

The common co-occurrence of the [100] and [1$\bar{1}$0] orientations (Fig. 6), accompanied by the appearance of half-integer $\frac{11}{22}$0-type reflections suggest the presence of superperiodicity along [110] (Fig. 5E, S4 and S7†). Our findings indicate that double periodicity along the [110]* direction could appear already in the nucleation stage (Fig. S3†). Some analogies can be drawn between aragonite and oxides: *in situ* TEM studies of iron oxides showed that either the same or twin crystallographic orientations are favoured during the particle attachment process.[43] Similarly, both parallel and twin assembly of nanoparticles have been reported for rutile.[32] In the case of aragonite, the Mg content of the solution appears to affect the particle attachment process, since Mg was suggested to be responsible for either the formation[57] or the enhancement of twin boundaries.[21] Thus, the non-integer reflections could possibly arise from nanoscale twinning or polytypism; however, neither could be confirmed from our HRTEM images in the studied projections.

Another feature observed in our products is the angular dispersion of reflections in SAED patterns, associated with mesocrystal assembly. The increasing angular length of 002 with increasing dissolved Mg : Ca ratio of the solution (Fig. 5A–C) possibly originates from the size reduction of the aragonite nanocrystals with the increasing Mg content (Fig. 4C). Interestingly, previous studies on biogenic aragonite (nacre) also reported that small misorientations of the [001] zone axis occurred,[58] suggesting that growth by particle attachment could be a prevalent strategy in biomineralization.[59,60] Moreover, Lew *et al.*[61] showed that the orientational differences between $CaCO_3$ nanocrystals could be essential for increasing the fracture toughness of the mineralized frameworks of corals, seashells and various other organisms. Our observations suggest that even without biological control or organic additives, simply the Mg content of the solution could affect the crystallographic texture of the product carbonate, in addition to controlling the polymorph selection. Thus, while our observations provide important details for a better understanding of the formation of mesoscopically ordered materials in abiotic systems, they also have implications for biomineralization processes.

Conclusions

Aragonite formation from Mg-rich aqueous solutions involves the precipitation of a transient form with a peculiar, spindle-shaped, aggregate-like appearance and mesocrystalline attributes. While our study focused on the properties and assembly of these spindles, our results also revealed the complexity of aragonite formation, and identified several stages in the process. We found that Mg-rich amorphous calcium carbonate (Mg-ACC) globules precipitate first from the solution. In the

next stage, elongated, few tens-of-nm-large aggregates of aragonite nanocrystals appear; we assume they form from Mg-ACC, and immediately merge and align along their *c*-axis, forming the nuclei of spindles. Then, further Mg-ACC particles are attached to the incipient spindles. Once the Mg-ACC particles reach the aragonite spindle, they transform into aragonite nanocrystals, with this transition accompanied by the loss of Mg, suggestive of a dissolution–reprecipitation process. As the process of attachment and conversion of Mg-ACC particles continues, the individual spindles develop into complex aggregates, consisting of two or more spindles, apparently intergrown in a crystallographically unspecified manner. In the last stage of aragonite formation, the morphology of the spindles is reshaped by Ostwald ripening, resulting in lath-shaped single crystals approaching the equilibrium crystal morphology of aragonite.

Aragonite spindles are also observed in biologically controlled mineralization, and their formation is typically attributed to the controlling effects of organic compounds. Our results show that spindle-shaped mesocrystal assemblies of aragonite can form in weak electrolyte solutions without organic additives. Instead of organics, the properties of aragonite mesocrystals, such as the development of the typical spindle morphology and the crystallographic coherence between their component nanocrystals, are affected by the presence and concentration of dissolved Mg^{2+} ions, respectively. These results imply a possible control mechanism by which living organisms could regulate the properties of the forming mesocrystals, bringing us a step closer to understanding aragonite biomineralization.

Author contributions

The manuscript was written by contributions from all authors. ZM initiated and planned the study, performed the precipitation experiments, characterized the products by TEM, interpreted the results and wrote the ms. PP performed electron tomography and processed its results. MP and AR were consulted during the entire study, contributed to the writing of the ms and secured funding. All authors have given approval to the final version of the manuscript.

Conflicts of interest

There are no conflicts to declare.

Acknowledgements

References

1 P. N. Gavryushkin, A. B. Belonshko, N. Sagatov, D. Sagatova, E. Zhitova, G. M. Krzhizhanovskaya, A. Rečnik, E. V. Alexandrov, I. V. Medrish, Z. I. Popov and K. D. Litasov, *Cryst. Growth Des.*, 2020, **21**(1), 65–74.
2 W. Sun, S. Jayaraman, W. Chen, K. A. Persson and G. Ceder, *Proc. Natl. Acad. Sci. U. S. A.*, 2015, **112**(11), 3199–3204.
3 B. Jones and X. Peng, *Sediment. Geol.*, 2016, **345**, 103–125.
4 R. Boch, X. Wang, T. Kluge, A. Leis, K. Lin, H. Pluch, F. Mittermayr, A. Baldermann, E. M. Böttcher and M. Dietzel, *Sedimentology*, 2018, **66**(2), 604–635.
5 Y. Fang, F. Hobbs, Y. Yang and H. Xu, *Sedimentology*, 2023, **70**(4), 1328–1347.
6 M. Boon, W. D. A. Rickard, A. L. Rohl and F. Jones, *Cryst. Growth Des.*, 2020, **8**, 5006–5017.
7 V. Mavromatis, J.-M. Brazier and K. Goetschl, *Geochim. Cosmochim. Acta*, 2021, **317**(15), 53–64.
8 A. J. Guiffre, C. A. D. Gagnon, J. J. De Yoreo and P. M. Dove, *Geochim. Cosmochim. Acta*, 2015, **165**, 407–417.
9 Z. Zhang, Y. Xie, X. Xu, H. Pan and R. Tang, *J. Cryst. Growth*, 2012, **343**, 62–67.
10 J. M. Walker, B. Marzec and F. Nudelman, *Angew. Chem., Int. Ed.*, 2012, **56**(39), 11740–11743.
11 Z. Molnár, P. Pekker, I. Dódony and M. Pósfai, *Earth Planet. Sci. Lett.*, 2021, **567**, 116971.
12 O. Nahi, N. Kulak, S. Zhang, X. He, Z. Aslam, M. A. Ilet, I. J. Ford, R. Darkins and F. C. Meldrum, *Adv. Sci.*, 2023, **10**(1), 2203759.
13 B. Jones, *Sediment. Geol.*, 2017, **353**, 64–75.
14 I. Lee, S. W. Han, H. J. Chou and K. Kim, *Adv. Mater.*, 2001, **13**(21), 1617–1620.
15 G.-T. Zhou, Q.-Z. Yao, J. Ni and G. Jin, *Am. Mineral.*, 2009, **94**, 293–302.
16 S. Shi, Z. Su, H. Wei and X. Chen, *J. Appl. Polym. Sci.*, 2010, **117**, 3308–3314.
17 K. K. Sand, J.-D. Rodriguez-Blanco, E. Makovicky, L. G. Benning and S. L. S. Stipp, *Cryst. Growth Des.*, 2011, **12**, 842–853.
18 L. Liu, J. Jiang and S.-H. Yu, *Cryst. Growth Des.*, 2014, **14**(11), 6048–6056.
19 M.-G. Willinger, J. Polleux, M. Antonietti, H. Cölfen, N. Pinna and N. Nassif, *CrystEngComm*, 2015, **17**, 3927.
20 I. B. Meić, J. Kontrec, D. D. Jurašin, B. N. Džakula, L. Štanjer, D. Lyons, M. D. Sikirić and D. Kralj, *Cryst. Growth Des.*, 2016, **17**, 1103–1117.
21 S. Fermani, N. B. Džakula, M. Reggi, G. Falini and D. Kralj, *CrystEngComm*, 2017, **19**, 2451–2455.

22 S.-H. Yu, H. Li, Q.-Z. Yao, S.-Q. Fu and G.-T. Zhou, *J. Environ. Chem. Eng.*, 2017, **5**(1), 893–905.

23 F. Konrad, B. Purgstaller, F. Gallien, V. Mavromatis, P. Gane and M. Dietzel, *J. Cryst. Growth*, 2018, **498**, 381–390.

24 B. R. Heywood and S. Mann, *Chem. Mater.*, 1994, **6**, 311–318.

25 K. W. Park, S.-J. Ko, S. W. Lee, K.-H. Cho, J.-W. Ahn and C. Han, *J. Cryst. Growth*, 2008, **310**, 2593–2601.

26 Z.-Q. Huang, G.-S. Zhang and Y. Tan, *J. Nanomater.*, 2019, 7328478.

27 Z. Han, R. Meng, H. Zhao, X. Gao, Y. Zhao, Y. Han, F. Liu, M. E. Tucker, J. Deng and H. Yan, *Front. Microbiol.*, 2023, **14**, 1078430.

28 A. Sugawara and T. Kato, *Chem. Commun.*, 2000, **6**, 487–488.

29 M. Niederberger and H. Cölfen, *Chem. Rev.*, 2008, **108**(11), 4332–4432.

30 H. Cölfen and M. Antonietti, *Angew. Chem., Int. Ed.*, 2005, **44**(35), 5576–5591.

31 Y.-Y. Kim, A. S. Schenk, J. Ihli, A. N. Kulak, N. B. J. Hetherington, C. C. Tang, W. W. Schmahl, E. Griesshaber, G. Hyett and F. C. A. Meldrum, *Nat. Commun.*, 2014, **5**, 1–14.

32 V. Jordan, U. Javornik, J. Plavec, A. Podgornik and A. Rečnik, *Sci. Rep.*, 2016, **6**, 24216.

33 M. Jehannin, A. Rao and H. Cölfen, *J. Am. Chem. Soc.*, 2019, **141**, 10120–10136.

34 G. Zhu, M. L. Sushko, J. S. Loring, B. A. Legg, M. Song, J. A. Soltis, X. Huang, K. M. Rosso and J. J. De Yoreo, *Nature*, 2021, **590**, 416–422.

35 T. M. Stawski, G. J. Smales, E. Scoppola, D. Jha, L. F. G. Morales, A. Moya, R. Wirth, B. R. Pauw, F. Emmerling and A. E. S. Van Driessche, *Proc. Natl. Acad. Sci. U. S. A.*, 2021, **118**(48), e2111213118.

36 S. Yu, H. Li, Q.-Z. Yao, S.-Q. Fu and G.-T. Zhou, *J. Environ. Chem. Eng.*, 2017, **5**, 839–905.

37 A. Knoll, *Rev. Mineral. Geochem.*, 2003, **54**(1), 329–356.

38 G. Müller, G. Irion and U. Förstner, *Naturwissenschaften*, 1972, **59**, 158–164.

39 D. L. Parkhurst and C. A. J. Appelo, *Book chapter in: U.S. Geological Survey Techniques and Methods*, 2013, book 6, ch. A43, p. 497.

40 B. Purgstaller, K. E. Goetschl, V. Mavromatis and M. Dietzel, *CrystEngComm*, 2019, **21**, 155–164.

41 Z. Molnár, I. Dódony and M. Pósfai, *Geochim. Cosmochim. Acta*, 2023, **345**, 90–101.

42 Y. Hiragi, S. Kachi, T. Takada and N. Nakanishi, *Bull. Chem. Soc. Jpn.*, 1966, **39**(11), 2361–2364.

43 Y.-S. Li, J. S. Church and A. L. Woodhead, *J. Magn. Magn. Mater.*, 2012, **324**(8), 1543–1550.

44 E. Loste, R. M. Wilson, R. Seshadri and F. C. Meldrum, *J. Cryst. Growth*, 2003, **254**(1–2), 206–218.

45 P. Bots, L. G. Benning, J.-D. Rodriguez-Blanco, T. Roncal-Herrero and S. Shaw, *Cryst. Growth Des.*, 2012, **12**(7), 3806–3814.

46 D. Li, M. H. Nielsen, J. R. I. Lee, C. Frandsen, J. Banfield and J. J. De Yoreo, *Science*, 2012, **336**, 1014–1018.

47 K. J. Davis, P. M. Dove and J. De Yoreo, *Science*, 2000, **290**(5494), 1134–1137.

48 R. L. Penn and J. F. Banfield, *Science*, 1998, **281**(5379), 969–971.

49 J. Baumgartner, A. Dey, P. H. H. Bomans, C. Le Coadou, P. Fratzl, N. A. J. M. Sommerdijk and D. Faivre, *Nat. Mater.*, 2013, **12**, 310–314.

50 L. Kuhrts, S. Prévost, D. M. Chevrier, P. Pekker, O. Spaeker, M. Egglseder, J. Baumgartner, M. Pósfai and D. Faivre, *J. Am. Chem. Soc.*, 2021, **143**(29), 10963–10969.

51 T. M. Stawski, A. Van Driessche, M. Ossiro, J.-D. Rodriguez-Blanco, R. Besselink and L. G. Benning, *Nat. Commun.*, 2016, **7**(1), 11177.

52 T. M. Stawski, H. M. Freeman, A. Van Driessche, J. Hövelmann, R. Besselink, R. Wirth and L. G. Benning, *Cryst. Growth Des.*, 2019, **19**(7), 3714–3721.

53 J. De Yoreo, P. U. P. A. Gilbert, N. A. J. M. Sommerdijk, R. L. Penn, S. Whitelam, D. Joester, H. Zhang, J. D. Rimer, A. Navrotsky, J. F. Banfield, A. F. Wallace, F. M. Michel, F. C. Meldrum, H. Cölfen and P. M. Dove, *Science*, 2015, **349**(6247), aaa6760.

54 J. C. Hopkins, R. Podgornik, W.-Y. Ching, R. H. French and V. A. Parsegian, *J. Phys. Chem. C*, 2015, **119**, 19083–19094.

55 Q. Wang, B. Yuan, W. Huang, H. Ping, J. Xie, K. Wang, W. Wang, Z. Zou and Z. Fu, *Natl. Sci. Rev.*, 2023, **10**(4), nwad014.

56 V. Jordan, V. D. B. C. Dasireddy, B. Likozar, A. Podgornik and A. Rečnik, *Cryst. Growth Des.*, 2018, **28**(8), 4484–4494.

57 P. Németh, E. Mugnaioli, M. Gemmi, G. Czuppon, A. Demény and C. Spötl, *Sci. Adv.*, 2018, **4**, eaau6178.

58 X. San, M. Gong, J. Wang, X. Ma, R. dos Reis, P. J. M. Smeets, V. P. Dravid and X. Hu, *Proc. Natl. Acad. Sci. U. S. A.*, 2022, **119**(14), e2122218119.

59 K. Benzerara, N. Menguy, N. M. Obst, J. Stolarski, M. Mazur, T. Tylisczak, G. E. Brown and A. Meibom, *Ultramicroscopy*, 2011, **111**, 1268–1275.

60 I. Polishchuk, A. A. Bracha, L. Bloch, D. Levy, S. Kozachkevich, Y. Etinger-Geller, Y. Kauffmann, M. Burghammer, C. Giacobbe, J. Villanova, G. Hendler, C.-Y. Sun, A. J. Giuffre, M. A. Marcus, L. Kundanati, P. Zaslansky, N. M. Pugno, P. U. P. A. Gilbert, A. Katsman and B. Pokroy, *Science*, 2017, **358**(6368), 1294–1298.

61 A. J. Lew, A. C. Stifler, A. Tits, C. A. Schmidt, A. Scholl, A. Cantamessa, L. Müller, Y. Delaunois, P. Compére, D. Ruffoni, M. J. Buehler and P. U. P. A. Gilbert, *Adv. Mater.*, 2023, **35**, 2300373.